Biophysical Journal
Article

Biophysical Society

Kinetics of Formation and Asymmetrical Distribution of Hsp104-Bound Protein Aggregates in Yeast

Camille Paoletti,[1] Sophie Quintin,[1] Audrey Matifas,[1] and Gilles Charvin[1,*]
[1]Development and Stem Cells Department, IGBMC, CNRS UMR 7104, INSERM U964, Université de Strasbourg, Illkirch, France

ABSTRACT Budding yeast cells have a finite replicative life span; that is, a mother cell produces only a limited number of daughter cells before it slows division and dies. Despite the gradual aging of the mother cell, all daughters are born rejuvenated and enjoy a full replicative lifespan. It has been proposed that entry of mother cells into senescence is driven by the progressive accumulation and retention of damaged material, including protein aggregates. This additionally allows the daughter cells to be born damage free. However, the mechanism underlying such asymmetrical segregation of protein aggregates by mother and daughter cells remains controversial, in part because of the difficulties inherent in tracking the dynamics and fate of protein aggregates in vivo. To overcome such limitations, we have developed single-cell real-time imaging methodology to track the formation of heat-induced protein aggregates in otherwise unperturbed dividing cells. By combining the imaging data with a simple computational model of protein aggregation, we show that the establishment of asymmetrical partitioning of protein aggregates upon division is driven by the large bud-specific dilution rate associated with polarized growth and the absence of significant mother/bud exchange of protein aggregates during the budded phase of the cell cycle. To our knowledge, this study sheds new light on the mechanism of establishment of a segregation bias, which can be accounted for by simple physical arguments.

INTRODUCTION

The accumulation of misfolded proteins into large aggregates is thought to impair normal cellular physiology and is a hallmark of many age-related degenerative diseases (1). Protein aggregation is also thought to play an important role in the normal aging process of unicellular organisms (2–4). In budding yeast, which divides asymmetrically, mother cells generate buds that become daughter cells after division. A mother cell can produce only a limited number of daughter cells, ~20–30, before it enters replicative senescence and ultimately dies (5); however, daughters of aging mothers are born with full replicative potential (6) and display normal physiology (7), implying the existence of an unknown rejuvenation process. The main hypothesis is that senescence is a consequence of the progressive accumulation in mothers of deleterious factor(s) that are not transmitted to their progeny (7). More recently, aging cells were shown to undergo a sharp transition into a slow replicative state, termed the senescence entry point, which suggests a threshold effect of the cellular response to the accumulated damage (8).

Over the last 15 years, several potential aging factors have been identified, including extrachromosomal rDNA circles (9) and dysfunctional mitochondria (10–12). In addition, carbonylated proteins have a tendency to accumulate and form amorphous aggregates within mother cells (2,13). The asymmetrical mother/daughter partitioning of such aggregates is directly controlled by the expression of protein chaperones and the pleiotropic longevity regulatory gene *SIR2* (13). More recent work providing important mechanistic insights into how aggregates are partitioned has been extensively debated and experimentally refined. Heat shock-induced protein aggregates (PAs) have been monitored and characterized indirectly using the green fluorescent protein (GFP)-tagged disaggregase Hsp104, which binds amorphous protein clusters. Previous studies suggested that PAs in the bud may undergo retrograde transport to the mother cell through tethering to polarized actin cables (14,15). These results led to the proposal that an active spatial protein quality control mechanism helps to maintain daughters aggregate free upon mitosis and might be involved in the rejuvenation process observed in the

Submitted August 4, 2015, and accepted for publication February 23, 2016.
*Correspondence: charvin@igbmc.fr
Editor: Rong Li.
http://dx.doi.org/10.1016/j.bpj.2016.02.034

progeny of aging mothers. This hypothesis was later challenged by Zhou et al., who did not observe biased transport of aggregates through the bud neck (16). Using quantitative measurements of aggregate diffusion, these authors also showed that PA retention within mother cells can be explained by physical arguments; that is, the slow and anomalous diffusive properties of these large structures within a confined environment makes their transport through the bud neck very unlikely over cell cycle timescales. This conclusion was further supported by a recent theoretical study investigating the transport properties of cellular materials in various cell biology contexts (17) and by experiments in bacteria that led to similar explanations (4,18). However, previous work has shown that amorphous PAs do not freely diffuse within the cytosol but, rather, are targeted to perinuclear or perivacuolar compartments called JUNQ (which is also referred to as INQ (19)) and IPOD (20,21), respectively. Therefore, tethering of PAs to these structures could explain the limited diffusive properties of the PAs and, importantly, drive their asymmetrical inheritance in yeast (21). A subsequent study also supported the idea that PA retention is mediated by their localization to subcellular organelles (22). In that study, PAs resulting from various proteotoxic stresses were shown to associate with the endoplasmic reticulum or mitochondria or at the interface of the two structures. In this model, asymmetrical segregation of mitochondria-bound PAs would result from the biased transport of mitochondria to the bud, a process that remains to be understood (22).

Therefore, our understanding of the mechanism of PA segregation clearly remains incomplete. Several independent factors may have contributed to this situation. For example, even when colocalization assays of the Hsp104-GFP-bound PAs with specific organelles are performed with high-resolution imaging techniques, the complex aggregation kinetics of misfolded proteins, which involves the recruitment of multiple chaperone proteins, is superposed on the dynamic behavior of cellular organelles (such as mitochondria). Similarly, it is still unclear whether PAs are formed directly on their target organelles, as proposed recently (22), or whether small PAs are formed and then fuse before their recruitment to specific compartments (21,23). This distinction may have important consequences for their ability to segregate between mother and bud. Previous studies have used one or more proteotoxic stresses to destabilize protein conformation or the protein quality control machinery, thereby triggering PA formation. The dynamics or localization of the PAs was then assessed following a recovery period (typically 30 min). Although it is essential to distinguish between the establishment and the maintenance of unequal PA localization, this distinction is generally not possible (except in (15,24)), and therefore most previous studies did not mark the budding state at the time the stressor is applied. Notably, the model of cytoskeleton-driven aggregate transport proposes an active mechanism of segregation between the mother and daughter cell (i.e., it addresses asymmetry establishment) (14), whereas all other studies have focused on the retention of preexisting PAs by mothers (i.e., they address asymmetry maintenance) (16). In addition, the question of resolution/clearance versus segregation of PAs cannot be distinguished by static snapshots of the aggregation pattern determined after cell recovery. There is thus a clear need for a specific methodology allowing cell fate to be monitored during and after the application of stress to untangle the contributions of the establishment, maintenance, and clearance of PAs to their biased segregation.

To overcome the technical limitations mentioned previously and to further understand the establishment of an unequal PA repartition in mother versus bud following temperature stress, we have developed an assay to monitor the kinetics of PA formation triggered by a rapid increase in temperature from 30°C to 38°C (hereafter referred to as temperature shift, TS) in real time with single-cell resolution under the microscope, as described previously (23). In combination with a computational model of protein aggregation, our data clearly reveal that the establishment of biased accumulation of PAs in mother/daughter cells arises from the polarized growth of the bud during the budded period of the cell cycle.

MATERIALS AND METHODS

Strains and plasmids

All strains were congenic to S288C. The strain carrying Hsp104-GFP was purchased from Invitrogen (Carlsbad, CA) and the *bni1* deletion mutant was from Euroscarf (Bad Homburg, Germany). The strain carrying the Cdc10-mCherry fusion was a gift from Jeremy Thorner (University of California, Berkeley, CA), and the preCox4-mCherry marker was generously provided by Dan Gottschling (Fred Hutchinson Cancer Research Center, Seattle, WA). The 2μ pESC-GAL1p:Ubc9^{ts}:mCherry -ura3 plasmid was a kind gift from Michel Toledano and was transformed into the Hsp104-GFP strain. Other strains were generated by crossing and were scored by tetrad dissection according to standard techniques.

Microfabrication

The microfluidic master for heat shock studies was made using reactive ion etching (Bosch process). Prototypic molds were replicated in epoxy. The microchannels were cast by curing polydimethylsiloxane (Sylgard 184,10:1 mixing ratio) and then covalently bound to a 24 × 50 mm coverslip using plasma surface activation (Diener, Jettingen, Germany).

Time-lapse microscopy

Freshly thawed cells were grown overnight at various final cell densities. In the morning, log phase cells (OD ~0.2–0.5) were transferred into the microfluidic device, and heat shock experiments were started 4–6 h later. The device was perfused with medium (synthetic complete with 2% glucose; SCD) throughout the experiment using a peristaltic pump (Ismatec, Wertheim, Germany; flow rate 25 μl/min). Cells were imaged using an inverted Zeiss Axio Observer Z1 microscope (Zeiss, Oberkochen, Germany). Focus was maintained using a custom focus search algorithm and commercial

focus stabilization hardware (Definite Focus; Zeiss). Fluorescence illumination was achieved using LED light (precisExcite, CoolLed, Andover, UK), and light was collected using a 100× N.A. 1.4 objective and an EM-CCD Luca-R camera (Andor, Belfast, UK). The camera was triggered on the precisExcite module using a transistor-transistor logic signal. We used an automated stage to follow up to five positions in parallel over the course of the experiment. Images were acquired every 3 min, and three z-stacks (with 1 μm spacing) were collected to image most of the foci within the cells while maintaining phototoxicity at a minimal level. Cells were followed for up to 12 h. For the experiment combining Hsp-104 foci and Ubc9^{ts}-mCherry observation, a similar protocol was applied as with Cdc10-mCherry, except that cells were perfused with synthetic complete medium –ura + raffinose 2% + galactose 2%, to induce Ubc9^{ts}-mCherry aggregate formation.

To control the temperature in the chip and to perform the temperature shift, we built a custom sample holder with thermoelectric modules and an objective heater with heating resistors (see Text S1 in the Supporting Material). Temperature control was achieved using a proportional-integral-derivative controller (5C7-195, Oven Industries, Mechanicsburg, PA).

Image analysis

Raw images were processed using custom software, called phyloCell, based on MATLAB (The MathWorks, Natick, MA) and the image-processing toolbox (8). This software features a comprehensive graphical user interface to perform segmentation/tracking and to introduce manual error corrections. The software is available for download on GitHub (https://github.com/gcharvin/phyloCell). In this study, the software was used to segment cell contours based on phase contrast images, to detect aggregates from fluorescence images, to track cells over time, and to measure the fluorescence within the cells. Relative fluorescence concentrations were obtained by normalizing total fluorescence to cell volume. We checked that cell volume scaled with projected area$^{3/2}$ using cytoplasmic Hsp104-GFP fluorescence measurements (under stress-free conditions) in mother cells and in buds of varying sizes (see Fig. S8). In addition, we checked that an Hsp104-GFP foci scales linearly with the aggregates size by using an independent Ubc9^{ts}-mCherry marker (Fig. S9), which has been extensively used to ectopically generate protein aggregates (22,23). Custom background subtraction was performed by measuring background within the cell cluster.

Drug treatment

During the course of a standard time lapse experiment, cycloheximide (C4859; Sigma Aldrich, St. Louis, MO) was perfused in the medium at various concentrations (2 μg/ml and 100 ng/ml), concomitantly with the temperature shift, to inhibit cell growth.

Mathematical model for establishment of asymmetry by cell growth

See Text S1 in the Supporting Material for the detailed model used to explain the establishment of PA asymmetry.

RESULTS

Unequal accumulation of PAs in mothers and buds following temperature shift

To overcome the technical limitations associated with the assessment of PA segregation bias in mothers versus buds, we developed, to our knowledge, a new strategy to track the kinetics of PA formation in real time at single-cell resolution. We expressed GFP fused with Hsp104, a heat stress-induced chaperone that associates with PAs, to visualize the formation of PA foci in cells growing in a microfluidic device (Figs. 1 *A* and S1). Whereas severe (42°C) heat shock induces a complete growth stall and requires a recovery period before cells are observed ((14,16)), a TS from 30°C to 38°C (*within minutes*, see Fig. S1, *C* and *D*) induced a brief and transient cell growth arrest but was sufficient to induce massive formation of PAs (Figs. 1 *B* and S2 *B*; Movie S1). Because the cell division process was not significantly affected during this procedure, we were able to investigate the establishment of PA segregation bias in budded cells by continuous observation of cell proliferation.

We quantified both the number of PA foci and their total fluorescence intensity over time using a custom MATLAB-based image-processing pipeline (Figs. 1 *C* and S3; Text S1 in the Supporting Material). The number of foci peaked at an average of 2.6 ± 0.1 foci/cell (n = 265 cells) at 10 min after TS and declined to 1.2 ± 0.05 foci/cell after 30 min, thus revealing the kinetics of fusion of small PAs into larger ones. The increase in foci number was concomitant with the increase in total foci fluorescence after subtraction of cytoplasmic fluorescence (Fig. 1 *C*).

To assess the respective accumulation of PAs in mother and bud in budded cells following TS, we used a Cdc10-mCherry fusion as a marker of budding (Fig. 1 *B*) and we measured the cellular concentration of PAs ([Fluo.], defined as the total fluorescence within foci divided by the computed cell volume, see Materials and Methods) in every mother/bud (M/B) pair present at TS and at several time points post-TS, including at division (Fig. 2, *A* and *B*). Immediately after TS, the PA concentration in buds ([B. Fluo.]) was slightly higher than in mothers ([M. Fluo.]) (Fig. 2 *B*, *left panel*), giving a [B. Fluo.]/[M. Fluo.] ratio of 1.6 (Fig. 2 *C*). Of importance, this finding allowed us to rule out the hypothesis that foci are preferentially formed in mothers. Although PA concentration increased in both compartments upon division (Fig. 2 *B*; $p < 3 \times 10^{-9}$ for both compartments), the [B. Fluo.]/[M. Fluo.] median ratio dropped significantly to 0.6 (Fig. 2 *C*; $p = 4 \times 10^{-5}$). This result clearly indicated that unequal concentrations of PAs in mother and bud arose during the budded phase of the cell cycle following TS.

Because these experiments were performed with unsynchronized cells, we reasoned that the degree of asymmetrical PA distribution might be strongly dependent on the phase of the cell cycle at the time of heat shock. Indeed, plotting the [B. Fluo.]/[M. Fluo.] ratio as a function of bud size at the time of the TS revealed that the segregation bias was much stronger for small-budded cells ([B. Fluo.]/[M. Fluo.] = 0.16) than for large-budded ones, in which the average [B. Fluo.]/[M. Fluo.] ratio was close to 1 (Fig. 2, *D* and *E*; Movie S2). We noticed that the time between TS and division displayed a strong negative

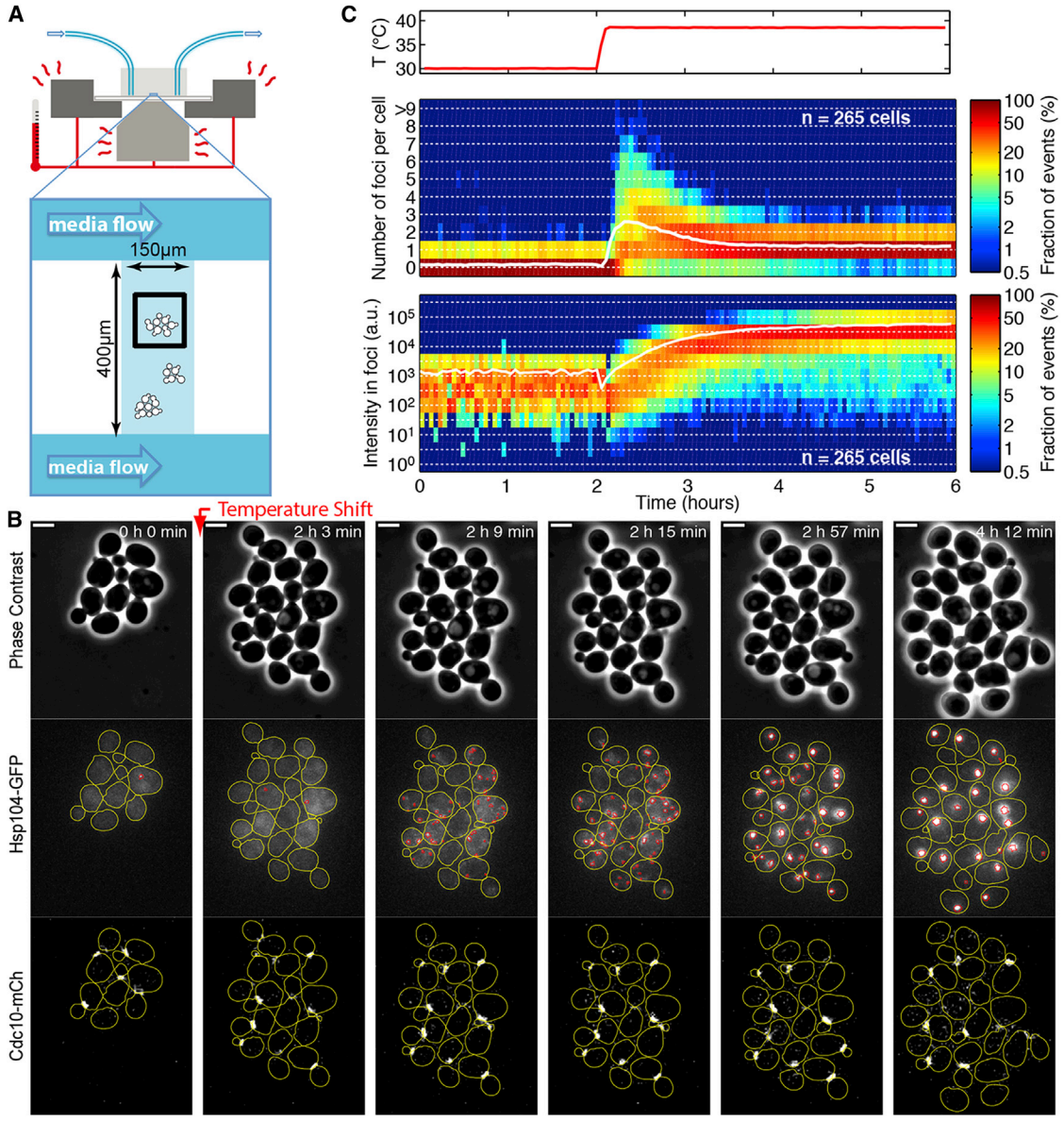

FIGURE 1 Monitoring formation of protein aggregates in real time following temperature shift. (*A*) Sketch of the experimental setup. Cells are grown in chambers on a microfluidic chip and fed by diffusion using media perfusion channels. Temperature shift is performed in situ with a custom heating stage and objective heater. (*B*) Sequence of phase contrast and fluorescence (Hsp104-GFP and Cdc10-mCherry) images obtained at the indicated times after initiation of heat shock by TS from 30°C to 38°C. On the fluorescence images, yellow and red lines represent the cell contours and the position of protein aggregates, respectively. Scale bar, 4 μm. (*C*) Quantification of the kinetics of protein aggregate induction. Upper panel: actual stage temperature over 6 h. Middle panel: two-dimensional histogram of the distribution of foci number per cell as a function of time. White line indicates the mean number of foci per cell. Lower panel: two-dimensional histogram of the distribution of total fluorescence intensity in foci as a function of time. White line indicates the mean fluorescence intensity. To see this figure in color, go online.

correlation with initial bud size, most likely because large-budded cells at the TS were close to division (Fig. 2 *F*). Regardless of the mechanism for establishing unequal PA concentration in mother and bud, the absence of asymmetrical segregation upon division of initially large-budded cells could reflect the shorter time during which segregation could occur.

To account for the cell-to-cell variability in PA repartition, we grouped single-cell data according to the initial bud size Vi (Fig. 2, *G–L*). We found that the time between TS and division of initially small-budded cells was longer than that of the large-budded cells, not only because of the growth requirements for completion of the cell cycle but also because, unexpectedly, the cells experienced a cell size-dependent transient growth arrest following TS (Figs. 2 *F*, *inset*, and *G*). Most importantly, the concentration of PAs was much lower in initially small buds (i.e., Vi $<$ 5 μm^3) than in larger ones (i.e., Vi $>$ 10 μm^3) (Fig. 2 *I*).

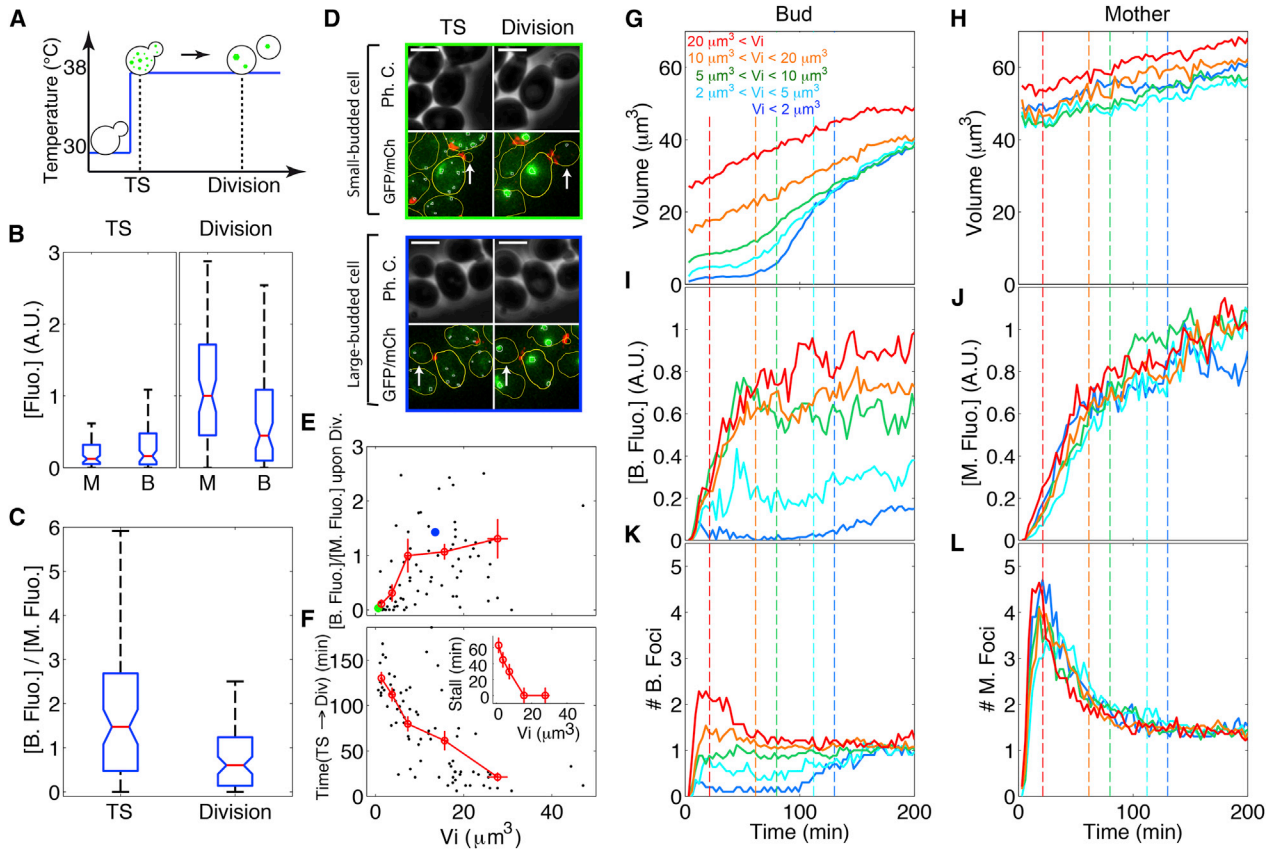

FIGURE 2 Establishment of unequal distribution of protein aggregates following temperature shift. (*A*) Sketch illustrating the TS assay and the specific time points at which PA concentration ([Fluo.]) was analyzed (*dotted lines*): 12 min after temperature shift (indicated by TS) and upon division. (*B*) Boxplots of PA concentration (measured as [Fluo.]; total fluorescence in foci/cell volume) in mothers (M) and buds (B) at the time points described in (*A*). The central red line indicates the median; the lower and upper box edges indicate the 25th and 75th percentiles, respectively; the notches indicate 5% confidence intervals; and the whiskers indicate the most extreme data points not considered outliers. (*C*) Boxplots of the ratio of [Fluo.] in bud versus mother at the same time points (see *B* for explanation). (*D*) Typical phase contrast and fluorescence images (*green*: Hsp104-GFP; *red*: Cdc10-mCherry) of small-budded (*upper*) and large-budded (*lower*) cells at the time points indicated in (*A*). Scale bar, 4 μm. (*E*) Median [B. Fluo.]/[M. Fluo.] ratio at division as a function of initial bud size at the time of TS. Black dots represent individual cells and red circles with error bars (statistical error on mean) display the same data after binning data by size. Green and blue dots correspond to the individual cells in the upper and lower panels shown in (*D*), respectively. (*F*) Time from TS to cell division for individual cells (*black dots*) and after binning (*red symbols*). Inset: growth arrest as a function of bud size upon TS. (*G–L*) Evolution with time of cell size (*G* and *H*), fluorescence concentration (*I* and *J*), and number of aggregates (*foci*) per cell (*K* and *L*) for the buds (*left column*) and the corresponding mothers (*right column*). Each colored line represents a group of individual time traces of mother-bud pairs grouped according to the initial volume of the bud Vi as indicated in the figure. Total number of cells analyzed = 78. Vertical dashed lines indicate the average time of division for each group of cells. To see this figure in color, go online.

This contrasted sharply with their mothers, which uniformly accumulated PAs (Fig. 2 *J*). Similarly, the average number of PAs in buds following TS was strongly dependent on the initial bud size (Fig. 2 *K*), but this was not observed with their mothers (Fig. 2 *L*). These data suggested that bud growth during the budded period of the cell cycle could determine the PA asymmetry upon division.

PA dilution induced by the polarized growth of the bud drives asymmetrical PA distribution upon division

To test this hypothesis, we turned to a computational model that integrated both the formation and the fusion of PAs and the dynamics of cell growth following TS. Whereas physical arguments based on limited diffusion in a crowded environment (4,17,18) or tethering to specific organelles (20,22) can successfully describe the maintenance of unequal PA concentration across the bud neck, it is important to note that none of them can explain how such a difference can emerge during the budding process. Therefore, we simulated the formation and fusion of PAs within a cell using a previously developed coalescence framework (25,26) that was recently used to model the distribution of PAs in fission yeast (25). The aggregation of misfolded proteins was represented by an aggregation kernel that describes the frequency of fusion of particles of different sizes (maximal radius of particles $a_{max} = 0.6$ μm (Fig. S4), constant rate

$k = 0.0035\ min^{-1}$; see Figs. S4 and S5; see Text S1 in the Supporting Material for details about the model and the determination of parameters value) in a cellular compartment of volume V. One major advantage of this strategy is that it bypasses the spatial description of aggregate diffusion, which is cumbersome and computationally intensive. Using the Gillespie algorithm, we computed the stochastic kinetics of PA accumulation in cellular compartments, assuming that the M/B size evolved according to Fig. 2, *G* and *H*.

We purposely neglected the diffusion of particles through the bud neck, in agreement with experimental observations as well as previous theoretical work, as described in the following: the equilibration of PA in mothers and buds was shown to be slow enough to not interfere with the kinetics of aggregation following heat shock (according to (16,17), only ~10% of PAs originally present in the mother cell are found in the bud after 90 min). In line with this, by scoring the number of foci transports from a bud to its mother over the course of the experiment (Fig. S6, *A* and *B*), we found that the frequency of these events was very low (11%, $n = 78$, Fig. S6 *C*). This hypothesis was also motivated by the observation that *bni1* mutants, which are defective in actin cable assembly, have an increased bud neck aperture (Fig. S7, *A* and *B*), and therefore a larger probability of PA escape, compared to wild-type yeast, but they display a comparable asymmetrical PA repartition ratio upon division (Fig. S7 *C*) and similar PA accumulation kinetics in mothers and buds as the wild-type strain (Fig. S7, *D–I*). Therefore, in this model, mother and bud were treated as independent cellular compartments, even though we could not exclude the possibility that small invisible particles may exchange across the bud neck.

For consistency with our experiments, we introduced a particle visibility threshold such that small PAs would be considered invisible until their size reached a fraction T of the size of the largest observed PAs (T ~0.01). We found that the formation of individual misfolded proteins should be modeled as a zeroth order process, the rate of which declines exponentially with time following TS (decay rate $\alpha = 0.011\ min^{-1}$). This assumption was necessary to fit the observation that the kinetics of the fluorescence increase in PAs was considerably slower than would be expected from the aggregation dynamics of particles if generated all at once following the TS. Finally, cell growth was modeled to reproduce the dynamics of the volume increase observed in buds of various initial sizes (Fig. 2 *G*). For the sake of simplicity, we assumed that the initial post-TS cell cycle stall was followed by exponential growth until the bud reached a fraction of the size of its mother, after which the growth rate was greatly reduced (see Text S1 in the Supporting Material for more details related to the model description).

Remarkably, we observed that such a simple framework (with only four experimentally constrained parameters related to PA formation: a_{max}, k, α, and T) was sufficient to quantitatively describe the evolution of the number and concentration of PAs as a function of time, both in buds of various initial sizes and in mother cells (Fig. 3, *A–C*). In particular, the model successfully captured the size dependence and lower concentration of PA fluorescence in bud versus mother (*colored* versus *black lines*, respectively, in Fig. 3 *B*), thus illustrating the asymmetry in PA distribution across the bud neck.

This nonintuitive behavior can be understood as the net result of several counteracting forces. First, the visibility threshold tends to make PAs invisible in tiny buds, which explains why fluorescence concentration is close to 0 when growth is stalled. Second, as PAs become increasingly visible, there is competition between the coalescence of newly unfolded proteins (which tend to increase the PA concentration) and the dilution due to cell growth (which decreases PA concentration). This latter effect seems to dominate the kinetics of PA accumulation and leads to a decrease in (or at least stabilization of) the PA concentration during the polarized growth phase of the cell cycle in a bud size-dependent manner (Fig. 3 *B*). Consistent with this, setting the growth rate to 0 in the simulation (Fig. 3 *D*), showed that the difference in PA concentration between mother and bud was fully abolished, except in tiny buds (Fig. 3 *E*).

Therefore, this computational simulation suggested that the dilution induced by bud growth may drive the unequal distribution of PAs in mother and bud. Consistently, by plotting the bud/mother ratio of PA concentration (at $t = 200$ min following TS) as a function of the mother/bud ratio of volume fold change between $t = 0$ and $t = 200$ min (referred to as the dilution factor), we observed that single-cell data grouped by initial bud volume were close to the diagonal (see *colored open circles* on Fig. 3 *G*). This suggested that concentration ratios could simply be set by the ratio of dilution factors.

To further support this conclusion, we used two independent strategies to perturb the polarized growth of the cell and therefore affect the dilution factor in the bud. First, we performed a TS experiment at 40°C. Unlike at 38°C, bud growth was almost completely arrested (Fig. S10) and, therefore, the mother/bud ratio of dilution factor measured for both small-budded cells and large-budded cells was close to 1 (see *colored open squares* on Fig. 3 *G*). However, we noticed that bud-to-mother transport events were much more frequent under these conditions (27% at 40°C vs. 11% at 38°C, $p = 0.018$, Fig. S6 *C*), with a strong dependency on the initial bud size (Fig. S6 *D*), due to bud growth arrest over a long time period. Whereas these transport events played a negligible role on the kinetics of PA accumulation at 38°C (Fig. S6, *E* and *G*), they lead to a significant underestimate of PA concentration at 40°C (Fig. S6, *F* and *H*). By filtering out the cells in which transport of foci occurred at 40°C, we found that the bud/mother

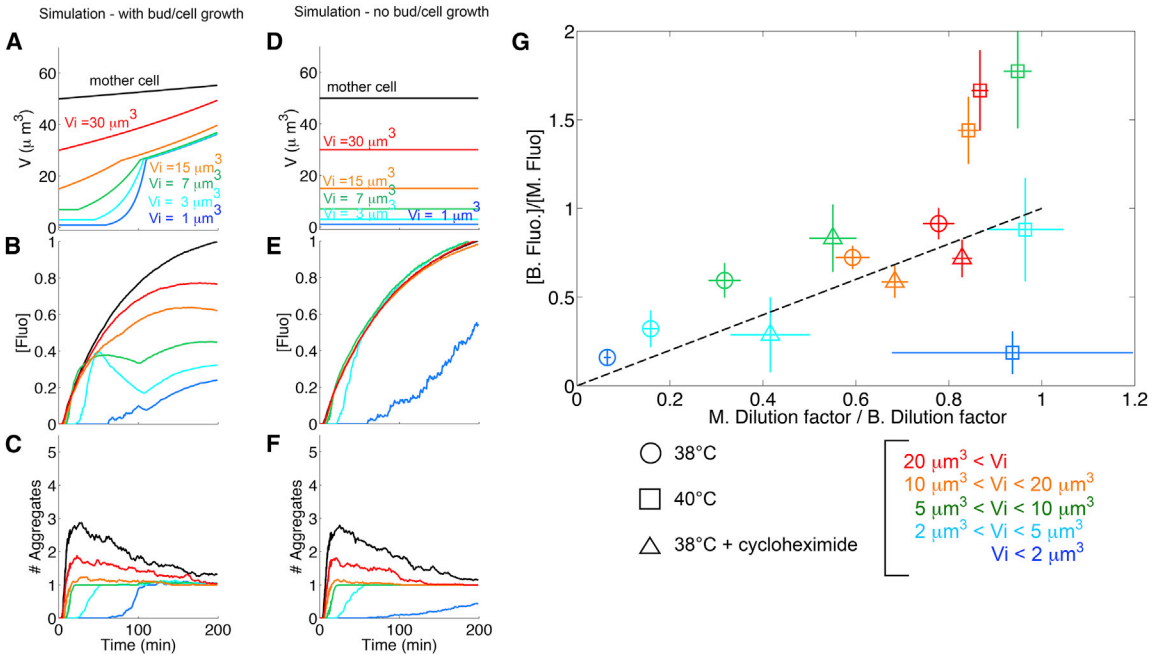

FIGURE 3 Effect of growth-induced dilution on mother/bud asymmetry in PA concentration: numerical model and experimental evidence. (*A–C*) Stochastic simulation of protein aggregation (all curves represent averages of 30 runs). Parameter values: $a_{max} = 0.6\ \mu m$; $\alpha = 0.02$; $T = 0.01$; and $k = 0.035\ min^{-1}$. (*A*) Cell volume as a function of time (cell growth is deterministic, and parameters for cell growth are set by the corresponding experimental curves in Fig. 2). Each colored line corresponds to a specific initial bud volume (Vi = 1,3,7,15, and 30 μm^3). The black line represents a mother cell of initial size 50 μm^3. See Supporting Material text for other parameter values. (*B*) Concentration of misfolded proteins in PAs as a function of time. Each colored line corresponds to a specific initial bud volume (1, 3, 7, 15, and 30 μm^3). The black line represents a mother cell of initial size 50 μm^3. (*C*) Evolution of number of aggregates as a function of time. Each colored line corresponds to a specific initial bud volume (1, 3, 7, 15, and 30 μm^3). The black line represents a mother cell of initial size 50 μm^3. (*D–F*) same as (*A*)–(*C*), but with growth rate set to 0. (*G*) Bud/mother ratio in PA concentration (measured at $t = 200$ min following the temperature shift) as a function of the M/B ratio in dilution factor (i.e., cell volume increase factor between $t = 0$ min and $t = 200$ min) for the indicated conditions: 38°C (*circles*), 40°C (*squares*), and 38°C + 130 ng/ml cycloheximide (*triangles*). Each colored point corresponds to a group of cells with initial volume Vi, as indicated on the figure legend. Error bars represent standard error of the mean. The dashed line represents the diagonal. To see this figure in color, go online.

ratio of PA concentration was close to 1 for most cell groups (except for tiny buds), providing a satisfying agreement with the dilution model. (Noteworthy, some ratio measurements are close to 1.5 on Fig. 3 *G*, which is quite consistent with the overall ratio measured right after TS, i.e., when dilution plays no role, see Fig. 2 *C*.)

Second, we used cycloheximide (CHX) to inhibit cell growth. A high dose of CHX (100 μg/ml) was reported to prevent the formation of heat shock-induced Hsp104-bound aggregates (22), a phenomenon that we could reproduce with a concentration as low as 2 μg/ml (*middle panel* in Fig. S10). However, lowering further the concentration of CHX to 100 ng/ml significantly impaired cell growth, yet did not prevent the formation of PAs (although at a lower level, see *bottom panel* Fig. S10). Here again, we found an overall good scaling between bud/mother concentration ratios and M/B dilution ratios. Of importance, Fig. 3 *G* revealed that the different data sets could all be accounted for by a simple dilution mechanism, even though the data were obtained in several conditions in which the kinetic parameters of aggregates formation may vary.

To confirm that bud growth plays an essential role in determining the unequal PA concentration across the bud neck, we postulated that the sharp switch from strongly polarized to unpolarized bud growth by the end of the S/G2 phase should markedly affect the dynamics of PA accumulation. To test this hypothesis, we performed an in silico synchronization of temporal traces with respect to cell division, to make the cell polarization switch more obvious. As in Fig. 2, cells were grouped by initial bud size. By restraining our analysis to a specific window around cell division (between 50 min before and 50 min after division), we found that the emergence of small foci (referred to as "nucleation" in the following) in initially small buds was concomitant with the switch to unpolarized growth (see *blue curves* in Fig. 4, *A* and *B*). In contrast, initially larger buds, which displayed no pronounced change in growth rate, also showed no significant change in the rate of PA accumulation (see *green curve* in Fig. 4 *B*). Interestingly, the nucleation of PAs in the bud before division was also consistently observed in dividing cells that were born long after the initial TS (Fig. 4 *C*; Movie S3), indicating that unfolded proteins were still being generated during maintenance at

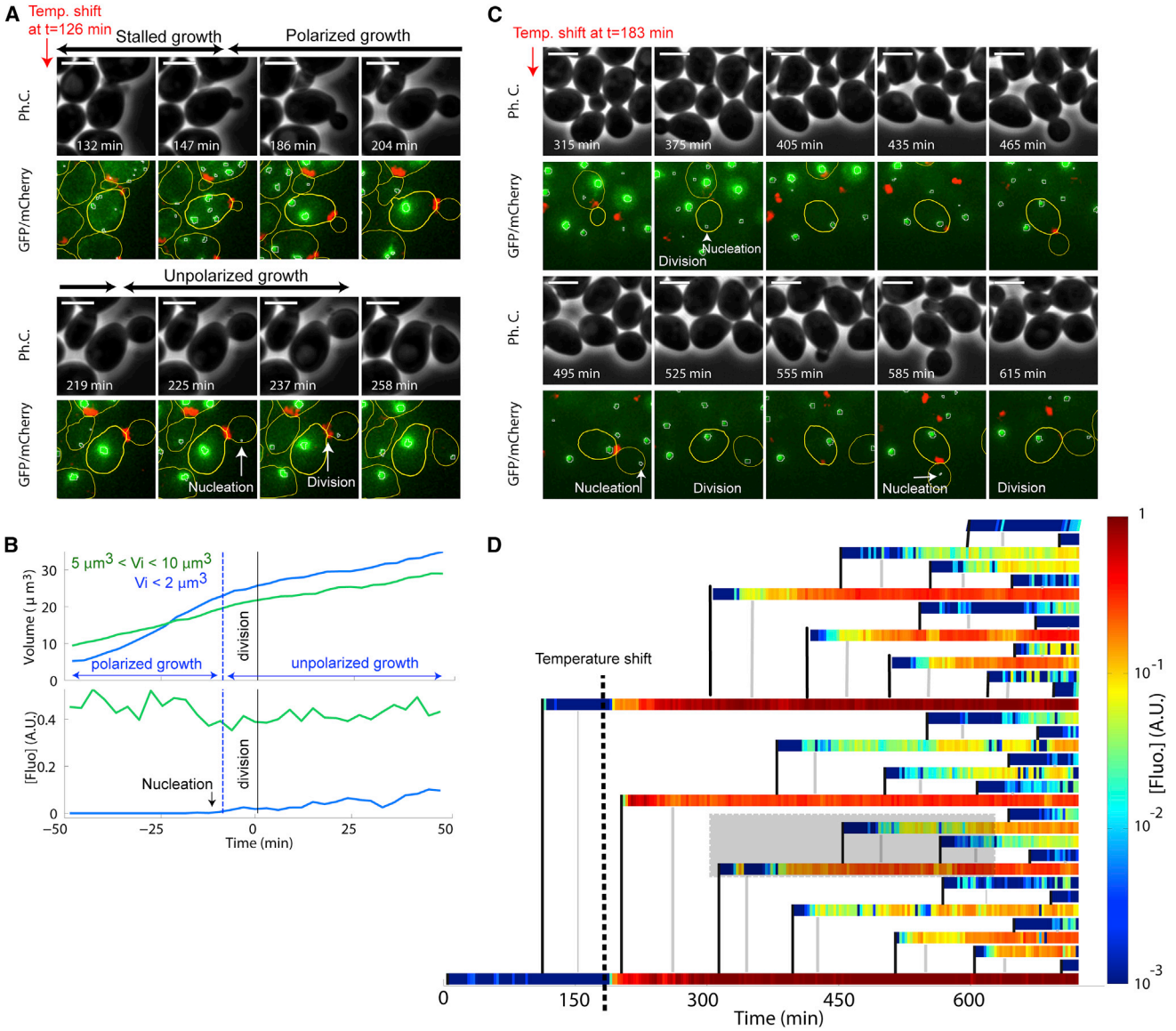

FIGURE 4 Nucleation of protein aggregates in growing buds. (*A*) Nucleation of small PAs during unpolarized bud growth. Sequence of images (phase contrast, overlaid Hsp104-GFP, and Cdc10-mCherry fluorescence) acquired at the indicated time points after TS (126 min). Scale bar, 4 μm. (*B*) Evolution with time of cell volume and [PA] after in silico synchronization with respect to cell division (indicated by the *solid black line*). Blue and green curves correspond to initially small and larger buds, respectively, as indicated. The dashed lines indicate the switch from polarized to nonpolarized growth for the initially small buds (*blue curve*). The onset of [Fluo] increase (nucleation) is indicated. (*C*) Successive nucleation of PAs in dividing cells following TS. Images are displayed as described in (*A*). (*D*) Pedigree of dividing cells before and following the TS (*black dashed line*). Each horizontal colored bar indicates the evolution of [PA] ([fluo] on a log scale; right vertical bar) as a function of time. The vertical solid black lines indicate the mother/daughter parentage and the onset of budding. The gray lines indicate the times of division. The gray box corresponds to the cell and its progeny displayed in (*C*). To see this figure in color, go online.

38°C. By quantifying the level of PA across a microcolony of growing cells, we found that successive buds of the founder cells were systematically free of PAs during their growth period, and nucleation of a small Hsp104-GFP focus occurred immediately before division (Fig. 4 *D*). Noteworthy, although PA concentration in founder cells converged to a very high level, cells that were born after the temperature switch reached a much lower plateau. These observations suggest that the rate of formation of misfolded proteins decreases over time, i.e., cells progressively adapt to elevated temperature.

Collectively, these results demonstrate that mother/daughter bias in PA accumulation is established by the strong dilution of PAs in the bud due to the polarized growth during the budded period of the cell cycle, as summarized in Fig. 5. The fact that none of the observed daughter cells (0 of 78 cells analyzed; Fig. 4 *D*) inherited a large aggregate from their mothers also confirmed that any

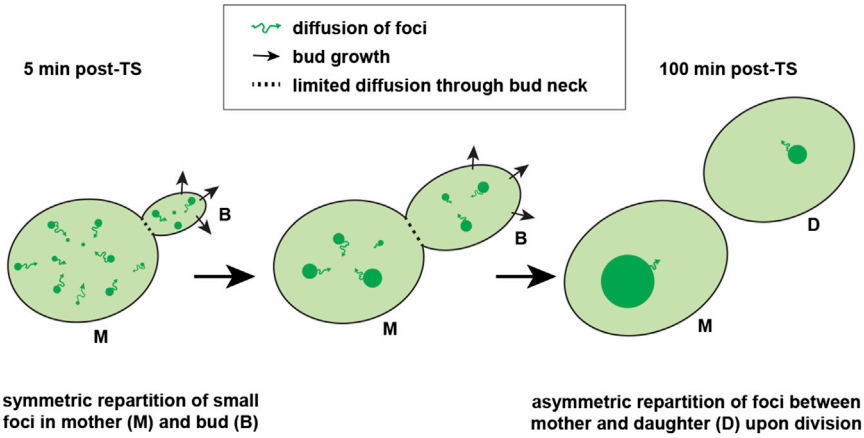

FIGURE 5 Schematic model describing the establishment of asymmetric protein aggregates repartition between mother and bud during cell cycle progression. Following an initial temperature shift (*left panel*), mother cell and bud share similar concentrations of small protein aggregates (PAs), depicted as green dots. These small PAs undergo random movements (*curly arrows*) and fuse together into larger structures (*middle panel*). Because of its polarized growth (*arrows*), PAs get more diluted in the bud than in the mother cell. This—as well as the limited diffusion of PAs through the bud neck (symbolized by the *dashed line*)—leads to unequal concentrations of PAs across the bud neck upon cell division. To see this figure in color, go online.

preestablished bias was maintained over a multigeneration timescale.

DISCUSSION

In this work, we combined quantitative live cell imaging, microfluidics, and a numerical simulation to investigate the establishment of asymmetrical segregation of heat shock-induced PAs between mother and daughter yeast cells. Unlike previous studies based either on static or on very short timescale analyses of the spatial partitioning of PAs and their interactions with subcellular organelles, we focused specifically on the real-time kinetics of PA accumulation in the cell cycle timescale. This approach, in which protein aggregation was observed concomitantly with the cell division process, allowed us to directly investigate contradicting models for the establishment and maintenance of the segregation bias.

Previous work has clearly demonstrated that slow and anomalous diffusion of PAs within cellular compartments prevents their passive transport to the bud on cell cycle timescales (16,17). Although the maintenance of asymmetrical segregation was proposed to result from the limited diffusion of these large inclusion bodies and their geometric constraints, the question of how biased PA accumulation is established has not been investigated using a limited set of physical arguments. We directly addressed this issue by monitoring the formation and fusion of PAs in unperturbed dividing cells. Both experimental and computational data clearly demonstrated that the Bud/Mother ratio in PA concentration depends on the initial bud size. Any quantitative description of the dynamics of PA concentration must necessarily take the dilution due to cell growth in account. Our analysis revealed that this sole physical argument is sufficient to explain the unequal partitioning of PAs across the bud neck, because the Bud/Mother PA ratio equals the Mother/Bud ratio in dilution factor (Fig. 3 *G*). Any additional mechanism generating an asymmetry (e.g., that would limit the level of PA concentration in the bud) should have further decreased the Bud/Mother PA ratio upon division below the level expected by the dilution model, contrasting with our observations. Therefore, although we cannot formally exclude the existence of such a bud-specific program, we anticipate that it would only have a minor contribution to the Bud/Mother PA ratio upon division. Rather, we conclude that a combination of bud growth and PA retention in the mother may be the main mechanisms leading to the establishment of unequal PA concentration across the bud neck (Fig. 5). This mechanism may also explain the unequal partitioning of aggregates in the mother versus daughter lineage on a multigeneration timescale (Fig. 4, *C* and *D*), which is consistent with the previous observation that the fraction of buds with aggregates decreases as a function of time following a temperature shift (14). Yet, our long-term single-cell imaging assay revealed that low PA concentration in daughters was the consequence of the absence of PA nucleation during most of the budding period (and cellular adaptation to high temperature), rather than resulting from an active retrograde transport (14).

In fission yeast, the fusion of aggregates into one unique structure promotes its asymmetrical segregation into one of the two sibling cells, leaving the other cell aggregate free (25). In our study, although PA fusion is responsible for a sharp slowdown in PA diffusion (see Fig. S4) and therefore is likely to limit transport through the bud neck, the main mechanism responsible for the differential accumulation of PAs is the polarized growth of the cell. We speculate that this mechanism, in combination with the large kinetic barrier associated with transport across the bud neck, may account for the bias observed in aggregates distribution between mother and daughters in an aging context.

Following initial studies proposing that PAs are recruited to various subcellular compartments (20), a growing body of evidence suggests that PAs generated by various proteotoxic stresses may be associated with mitochondria (22) and the endoplasmic reticulum (23,27). Our data indicate that the aggregation process can be accurately described using a coalescence model based on free particle diffusion. These

two a priori conflicting descriptions of aggregation can be reconciled by noting that mitochondria undergo very dynamic fusion/fission events, such that the apparent dynamics of PAs resembles that of freely diffusing particles (with low diffusion coefficients). To refine this analysis, further quantitative studies will be necessary to precisely determine whether the kinetics of PA fusion is limited by the diffusion of particles in a crowded environment or by the intrinsic dynamics of the mitochondrial network. Regardless, it is striking that the differential accumulation of PAs between mother and daughter can be simply described using a limited set of physical arguments and experimentally constrained parameters. Our work highlights the power of microfluidics-based single-cell assays to test and refine existing models of asymmetrical segregation of protein aggregates.

SUPPORTING MATERIAL

Supporting Materials and methods, ten figures, and three movies are available at http://www.biophysj.org/biophysj/supplemental/S0006-3495(16)300035-2.

AUTHOR CONTRIBUTIONS

C.P. and G.C. designed the project. C.P. performed most experiments; S.Q. and A.M. contributed additional experiments requested by reviewers. C.P. and G.C. analyzed the data. G.C. developed the numerical model. G.C. and C.P. wrote the article and S.Q. edited the manuscript.

ACKNOWLEDGMENTS

We thank Youlian Goulev for help with statistical analyses and the whole G.C. laboratory for careful reading of the manuscript. We thank Michel Toledano for reagents and useful discussions.

G.C. was supported by the ATIP-AVENIR program and C.P. was funded by a fellowship from the French Ministry of Higher Education and Research.

REFERENCES

1. Lindner, A. B., and A. Demarez. 2009. Protein aggregation as a paradigm of aging. *Biochim. Biophys. Acta.* 1790:980–996.
2. Aguilaniu, H., L. Gustafsson, …, T. Nyström. 2003. Asymmetric inheritance of oxidatively damaged proteins during cytokinesis. *Science.* 299:1751–1753.
3. Lindner, A. B., R. Madden, …, F. Taddei. 2008. Asymmetric segregation of protein aggregates is associated with cellular aging and rejuvenation. *Proc. Natl. Acad. Sci. USA.* 105:3076–3081.
4. Winkler, J., A. Seybert, …, B. Bukau. 2010. Quantitative and spatio-temporal features of protein aggregation in *Escherichia coli* and consequences on protein quality control and cellular ageing. *EMBO J.* 29:910–923.
5. Mortimer, R. K., and J. R. Johnston. 1959. Life span of individual yeast cells. *Nature.* 183:1751–1752.
6. Kennedy, B. K., N. R. Austriaco, Jr., and L. Guarente. 1994. Daughter cells of *Saccharomyces cerevisiae* from old mothers display a reduced life span. *J. Cell Biol.* 127:1985–1993.
7. Egilmez, N. K., and S. M. Jazwinski. 1989. Evidence for the involvement of a cytoplasmic factor in the aging of the yeast *Saccharomyces cerevisiae*. *J. Bacteriol.* 171:37–42.
8. Fehrmann, S., C. Paoletti, …, G. Charvin. 2013. Aging yeast cells undergo a sharp entry into senescence unrelated to the loss of mitochondrial membrane potential. *Cell Reports.* 5:1589–1599.
9. Sinclair, D. A., and L. Guarente. 1997. Extrachromosomal rDNA circles–a cause of aging in yeast. *Cell.* 91:1033–1042.
10. Hughes, A. L., and D. E. Gottschling. 2012. An early age increase in vacuolar pH limits mitochondrial function and lifespan in yeast. *Nature.* 492:261–265.
11. McFaline-Figueroa, J. R., J. Vevea, …, L. A. Pon. 2011. Mitochondrial quality control during inheritance is associated with lifespan and mother-daughter age asymmetry in budding yeast. *Aging Cell.* 10:885–895.
12. Veatch, J. R., M. A. McMurray, …, D. E. Gottschling. 2009. Mitochondrial dysfunction leads to nuclear genome instability via an iron-sulfur cluster defect. *Cell.* 137:1247–1258.
13. Erjavec, N., L. Larsson, …, T. Nyström. 2007. Accelerated aging and failure to segregate damaged proteins in Sir2 mutants can be suppressed by overproducing the protein aggregation-remodeling factor Hsp104p. *Genes Dev.* 21:2410–2421.
14. Liu, B., L. Larsson, …, T. Nyström. 2010. The polarisome is required for segregation and retrograde transport of protein aggregates. *Cell.* 140:257–267.
15. Liu, B., L. Larsson, …, T. Nyström. 2011. Segregation of protein aggregates involves actin and the polarity machinery. *Cell.* 147:959–961.
16. Zhou, C., B. D. Slaughter, …, R. Li. 2011. Motility and segregation of Hsp104-associated protein aggregates in budding yeast. *Cell.* 147:1186–1196.
17. Kinkhabwala, A., A. Khmelinskii, and M. Knop. 2014. Analytical model for macromolecular partitioning during yeast cell division. *BMC Biophys.* 7:1–10.
18. Coquel, A.-S., J.-P. Jacob, …, H. Berry. 2013. Localization of protein aggregation in *Escherichia coli* is governed by diffusion and nucleoid macromolecular crowding effect. *PLOS Comput. Biol.* 9:e1003038.
19. Miller, S. B. M., A. Mogk, and B. Bukau. 2015. Spatially organized aggregation of misfolded proteins as cellular stress defense strategy. *J. Mol. Biol.* 427:1564–1574.
20. Kaganovich, D., R. Kopito, and J. Frydman. 2008. Misfolded proteins partition between two distinct quality control compartments. *Nature.* 454:1088–1095.
21. Spokoini, R., O. Moldavski, …, D. Kaganovich. 2012. Confinement to organelle-associated inclusion structures mediates asymmetric inheritance of aggregated protein in budding yeast. *Cell Reports.* 2:738–747.
22. Zhou, C., B. D. Slaughter, …, R. Li. 2014. Organelle-based aggregation and retention of damaged proteins in asymmetrically dividing cells. *Cell.* 159:530–542.
23. Escusa-Toret, S., W. I. M. Vonk, and J. Frydman. 2013. Spatial sequestration of misfolded proteins by a dynamic chaperone pathway enhances cellular fitness during stress. *Nat. Cell Biol.* 15:1231–1243.
24. Hill, S. M., X. Hao, …, T. Nyström. 2014. Life-span extension by a metacaspase in the yeast *Saccharomyces cerevisiae*. *Science.* 344:1389–1392.
25. Coelho, M., S. J. Lade, …, I. M. Tolić. 2014. Fusion of protein aggregates facilitates asymmetric damage segregation. *PLoS Biol.* 12:e1001886.
26. Laurenzi, I. J., J. D. Bartels, and S. L. Diamond. 2002. A general algorithm for exact simulation of multicomponent aggregation processes. *J. Comput. Phys.* 177:418–449.
27. Song, J., Q. Yang, …, T. Nyström. 2014. Essential genetic interactors of SIR2 required for spatial sequestration and asymmetrical inheritance of protein aggregates. *PLoS Genet.* 10:e1004539.

Biophysical Journal, Volume *110*

Supplemental Information

Kinetics of Formation and Asymmetrical Distribution of Hsp104-Bound Protein Aggregates in Yeast

Camille Paoletti, Sophie Quintin, Audrey Matifas, and Gilles Charvin

Kinetics of formation and segregation bias of Hsp104-bound protein aggregates in single dividing yeast cells

C. Paoletti, S. Quintin, A. Matifas, and G. Charvin

Supporting information & supporting figures

Text S1. Extended experimental procedures and model description

Strain List

Name	MAT	Background	Genotype	Origin
YCP03-1	a	S288C	*his3Δ1 leu2Δ0 lys2Δ0 met15Δ0 ura3Δ0 HSP104-GFP-HIS3MX6 CDC10-mCherry-kanMX4*	This study
YCP09-1	a	S288C	*his3Δ1 leu2Δ0 lys2Δ0 met15Δ0 ura3Δ0 HSP104-GFP-HIS3MX6 CDC10-mCherry-kanMX4 bni1Δ-KanMX4*	This study
YCP21-7D	a	S288C	*his3Δ1 leu2Δ0 lys2Δ0 met15Δ0 ura3Δ0 HSP104-GFP-HIS3MX6 HTB2-mCherry-kanMX4*	This study
YCP19-8D	a	Mix S288C / SEY6210	*HSP104-GFP-MX6 VPH1-mCherry-TRP1*	This study
YSQ01-A	a	YLL026W	*HSP104-GFP; 2μ pGAL1p-Ubc 9^{ts}-mCherry*	This study

Maintenance of focus during heat-shock experiments

All microscope parts and the sample holder undergo significant dilatation as the temperature is changed. This phenomenon has important implications for the maintenance of focus during rapid temperature changes. By using a Definite Focus (Zeiss) system to maintain a constant distance between the objective and the chip, we observed a drift of the focal plane by up to 23 μm during an abrupt temperature switch (TS) (Fig. S1C). Therefore, we combined the Definite Focus system hardware with homemade MATLAB software to maintain a constant distance between the objective and the chip, thereby allowing cells to be monitored during the TS.

Computational model of protein aggregation in dividing cells

The purpose of the computational model is to investigate whether the establishment of PA concentration asymmetry during the budded period of the cell cycle can be explained using a limited set of physical arguments. Therefore, hypotheses are included in the model in a sequential manner in order to understand the role of each specific feature.

Principle of the model

To model the aggregation kinetics of misfolded proteins into large protein clusters, we used the numerical framework described by [1] and later used by [2] to evaluate the distribution of PAs in fission yeast. In brief, the simulation is based on an exact stochastic simulation that derives from the Gillespie algorithm and models all possible reactions between the different species (i.e., PAs of different sizes). To this end, the simulation uses an aggregation kernel K(i,j) [3] that quantifies the frequency of collision between PAs of radius a_i and a_j:

$$\text{Frequency of aggregation} = K(i,j)\, N(i)\, N(j) \qquad \text{(Eq. 1)}$$

where N(i) and N(j) are the number of aggregates of radius a_i and a_j, and $K(i,j) = \frac{4\pi}{V}\left(D_i + D_j\right)(ai + aj)$, where D_i and D_j are the diffusion coefficients of particles of size a_i and a_j respectively [4], and V is the volume of the compartment.

We set N particles at the beginning of the simulation and we let the population of aggregates evolve due to fusion (and nucleation, see below) events that stochastically occur according to the Gillespie algorithm. Upon fusion of particles of size a_i and a_j, a new particle of size $\left({a_i}^3 + {a_j}^3\right)^{1/3}$ is generated, and the number of particles of size a_i and a_j decreases by 1. For each simulation step, as the number of aggregates evolves, the kinetic constants associated with aggregation of each particle are recomputed. This algorithm is iterated until all particles are aggregated or until the total duration reaches a set value (usually 200 min).

A major advantage of this framework is that it bypasses the need to simulate the spatial diffusion and collision of aggregates, which is computationally intensive because the two processes occur over very different timescales for particles of varying sizes.

A - Aggregation frequency

If we assume that aggregates follow the Stokes-Einstein equation: $D_i = \frac{k_B T}{6\,\pi\,\mu\,a_i}$

where k_B is the Boltzmann constant, T is the temperature, V is the volume of the compartment, and μ is the viscosity of the medium, then the aggregation kernel K can be rewritten as:

$$K(i,j) = \frac{2\,k_B\,T}{3\,V\,\mu}\left(\mathrm{a}_i + \mathrm{a}_j\right)\left({\mathrm{a}_i}^{-1} + {\mathrm{a}_j}^{-1}\right) \qquad \text{(Eq. 2)}$$

This is known as the Smoluchowski equation for coalescence of Brownian particles. An important feature of this formula is that only the ratio of particle size a_i/a_j is important for determining the order of

magnitude of the aggregation kinetics. Therefore, no absolute size scale related to particle size appears in this formula.

By measuring the diffusion coefficient of particles of various sizes using mean square displacement analysis at different times following the TS (using mean square displacement analysis in confocal microscopy), we found that $D_i = \frac{\beta}{a_i{}^{\gamma}}$ yields the best fit with β =1.4 × 10^{-4} and γ = -2.1, thus ruling out the hypothesis that PAs behave according to the Stokes-Einstein equation (Fig. S4). Therefore, by making the approximation that γ ~ -2, the aggregation kernel used in the simulation becomes:

$$K(i,j) = \frac{4\pi\,\beta}{V}\left(a_i + a_j\right)\left(a_i{}^{-2} + a_j{}^{-2}\right) \quad \text{(Eq. 3)}$$

Therefore, Eq. 3 features an absolute size scale for aggregating particles. Since there is conservation of the total volume of particles within aggregates, and N is the initial number of particles, the size of the initial particles is set to $a_1 = a_{max}/N^{1/3}$, where the maximum size of an aggregate a_{max} can be deduced from experiments: a_{max} ~ 0.6 μm (Fig. S4). Therefore, the kernel can be rewritten as:

$$K(i,j) = k\left((m_i/N)^{1/3} + (m_j/N)^{1/3}\right)\left((m_i/N)^{-2/3} + (m_j/N)^{-2/3}\right)$$

where m_i and m_j are the volumes of particles i and j ($1 < m_i < N$), and $k = \frac{4\pi\,\beta}{V\,a_{max}}$. Assuming V = 50 μm^3 (mean cell volume of yeast cells) yields k = 3.5 10^{-3} min^{-1}.

Fig. S5A shows the evolution of the number of aggregates with time resulting from the simulation described above, starting with a number N = 1000 particles. As expected, the kinetics of aggregation greatly depends on the aggregation rate k (colored lines on Fig. S5A). Importantly, the theoretical value k = 3.5 10^{-3} min^{-1} calculated from Eq. 3 provides a decent fit with the decay in aggregate number observed in the experimental data, even though it tends to underestimate the number of aggregates on timescales of >30 min (black line on Fig. S5A).

B- Initial number of particles

Since the maximal size of the largest aggregate is set to a constant value a_{max}, changing the number of initial particles N only affects the size of the initial particles: $a_1 = a_{max}/N^{1/3}$. Therefore, we expect this parameter to have no influence on the kinetics of aggregate fusion on long timescales. Indeed, using N between 50 and 5000, we saw no significant change in the kinetics of aggregation (Fig. S6B). Interestingly, this implies that the aggregation process is independent of the initial particle size and therefore of the nature of the proteins involved in the aggregation.

C- Aggregate visibility threshold

Our experiments showed that the number of visible aggregates increased during the first 20 min after the TS and then decreased to ~1/cell as they fused into larger structures (see Fig. 2 in the main text).

This non-monotonous variation in the aggregate number occurs because small aggregates formed immediately after the TS were too dim and/or diffused too rapidly to be detected experimentally.

To include this feature in the model, we introduced a visibility threshold T ($0 < T < 1$) so that any aggregate of volume smaller than $T\ a_{max}^3$ was invisible (Coelho et al. 2014). As expected, both the timing and the peak number of aggregates greatly depended on T (Fig. S6C), and higher T tended to decrease the height of the peak in the kinetics of aggregation.

T can be viewed as the volume ratio of the smallest detectable aggregate to the largest observed aggregate. We found that T ~0.1 provided the best agreement with the experimental data (Fig. S6C), suggesting that foci fluorescence intensity by the end of the aggregation process should be no more than 10 times that of the smallest foci (detected before or during the TS). However, our experiments directly contradicted this, yielding a ~100-fold difference in foci intensity before and after the TS (Fig. 1C in the main text), suggesting that an additional factor was setting the shape of the experimental aggregation kinetics, as described below.

D - Kinetics of formation of misfolded proteins

In addition to the kinetics of aggregate number described above, we focused on the PA concentration within cells as a function of time. We found that the experimental kinetics of aggregate accumulation was very different from that observed in the simulation. By the time the aggregate number peaked (red dashed line in Fig. S5D, E), <10% of the final PA fluorescence concentration had been reached experimentally (black curve) versus >75% in the simulation (green curve).

This delay in the accumulation of PAs could not be attributed to the time for Hsp104-GFP protein maturation, since they were already present upon TS. Up to this point in the simulation, we have considered that misfolded proteins were all generated at the time of the TS. However, the observation that the kinetics of aggregate number and fluorescence differed experimentally suggests that the kinetics of protein misfolding – rather than the kinetics of aggregate emergence above the visibility threshold due to particle fusion – may set the timescale for aggregate accumulation. Therefore, we modelled this using zeroth-order kinetics of formation of misfolded proteins, the rate k_m of which decays exponentially with time (per unit of volume) as follows:

$$k_m = k_0\, e^{-\alpha t}$$

where k_0 is the initial rate of formation and α sets the timescale for the decay in misfolded protein formation. This requires only one additional parameter, since k_0 and α are linked to the total number of misfolded proteins N by:

$$N = \int_0^\infty k_m\, V\, dt \approx\ k_0\, V/\alpha$$

assuming a constant volume during the course of the experiment. By fitting an exponential curve to the fluorescence accumulation kinetics (gray dashed line in Fig. S5E), we obtained α = 0.011 min^{-1}

and we input this parameter in the simulation. As expected, the simulation accurately reproduced the experimental data for both aggregate concentration (Fig. S5E) and number (Fig. S5D). The agreement of the simulation with the experimental data was quite sensitive to the value of α, indicating that this parameter describes an essential feature of the aggregation kinetics.

The experimental kinetics of aggregate number was also captured well by the simulation, in which each parameter was either determined by the fit to experimental data or was derived from theoretical considerations —see below.

E- Parameter values

Parameter name	Value	Comment
a_{max}	0.6 μm	Maximal radius of aggregates;
k	3.5 10^{-3} min^{-1}	Aggregation frequency; estimated in section A above, knowing cell volume V and a_{max}
T	0.01	Aggregate visibility threshold (section C above); estimated from the ~100-fold difference in foci intensity before and after the TS (Fig.1C)
α	0.011 min^{-1}	Decay rate for the formation of unfolded proteins following TS (section D above); obtained by fit to the experimental data (Fig. S5E)
N	1000	Total number of aggregated proteins during the assay (section D). This arbitrary parameter sets the magnitude of the aggregation process, yet it plays no role in the aggregation kinetics (See Fig. S5B).

F- Effect of cell size and growth on aggregation kinetics

Having investigated the agreement between the model and the experimental aggregation kinetics using data obtained for mother cells, we wondered whether the model would predict the aggregation kinetics in buds, which have smaller and more variable initial volumes (typically V ~1–30 μm^3).

Interestingly, the evolution of the aggregate number in buds was in good agreement with the experimental data; the number of particles as a function of time was greatly modified in smaller compartments (Fig. 3F). This is due to the fact that the mean size of aggregates is smaller in smaller cells, which makes them more likely to fall below the visibility threshold T.

However, the aggregate concentration in the bud seems to be independent of the bud size, which

contradicts the experimental data (with the exception of tiny buds, see Fig. 3E). This apparent contradiction is a consequence of maintaining a constant bud size throughout the simulation. By taking bud growth into account (as observed in Fig. 2G), we could recapitulate the kinetics of PA concentration (see main text and Fig. 3A–C).

Additional Bibliography

[1] Laurenzi, I.J., Bartels, J.D., and Diamond, S.L. (2002). A general algorithm for exact simulation of multicomponent aggregation processes. J Comp Phys *177*, 418–449.

[2] Coelho, M., Lade, S.J., Alberti, S., Gross, T., and Tolić, I.M. (2014). Fusion of protein aggregates facilitates asymmetric damage segregation. PLoS Biol *12*, e1001886.

[3] Hidy G.M., Brock, J.R. (1972). Topics in current aerosol research, Pergamon press.

[4] Friedlander, Sheldon K. (2000). Smoke, dust, and haze: fundamentals of aerosol dynamics, Oxford University Press.

Movie legends

Movie S1. Refers to Fig. 1. Cells undergoing the temperature shift from 30°C to 38°C at t = 2 h. Overlay of phase contrast and Hsp104-GFP (green) images. Scale bar: 4 μm.

Movie S2. Refers to Fig. 2. Differential accumulation of protein aggregates in mothers and buds for initially small-budded cells upon temperature shift from 30°C to 38°C at t = 2 h. The fluorescence signal corresponds to Hsp104-GFP. Lines represent cell and foci contours. Scale bar: 4 μm

Movie S3. Refers to Fig. 4. Nucleation of protein aggregates in daughter cells grown at 38°C over multiple generations. The fluorescence signal corresponds to Hsp104-GFP. Lines represent cell and foci contours. Scale bar: 4 μm

Supporting figures

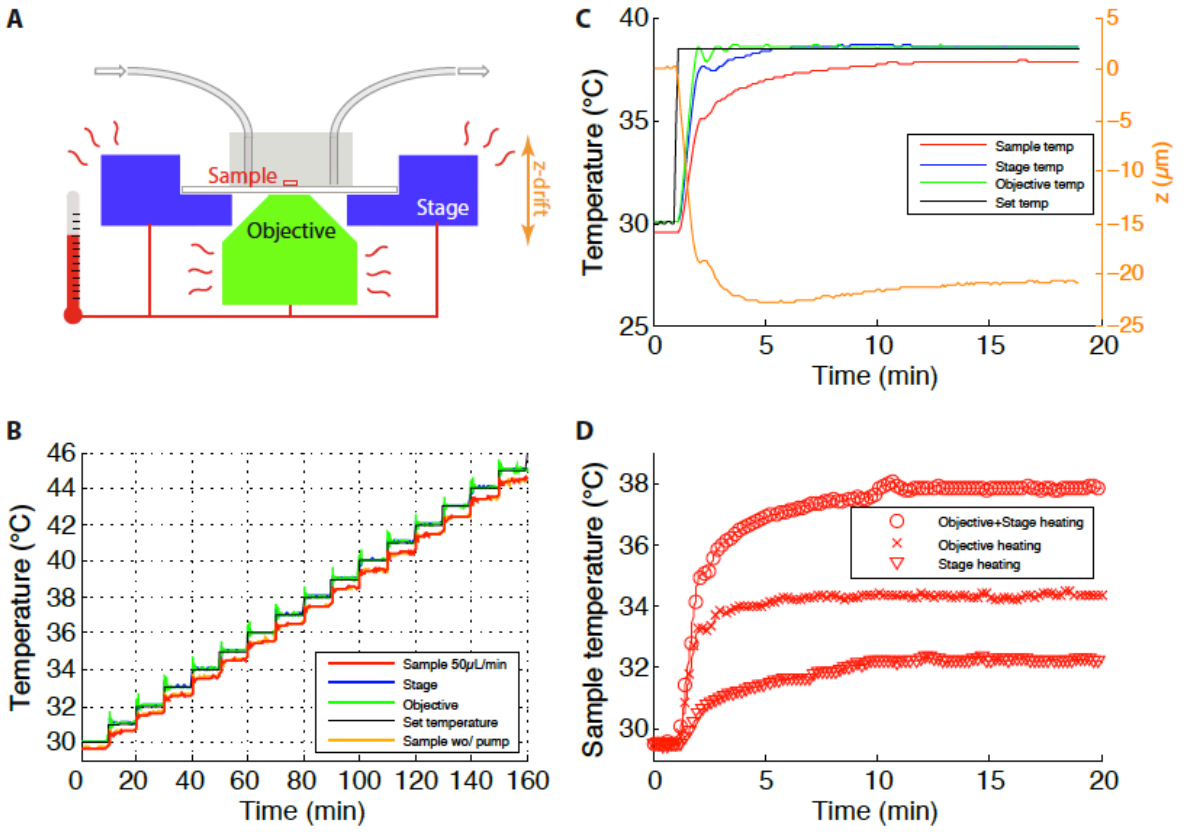

Figure S1. Sketch of the heating stage and calibration of sample temperature

(A) Sketch of the setup developed to control the sample temperature during temperature shift (TS) experiments. We built a custom sample holder (blue) with thermoelectric modules and an objective heater (green) with heating resistors. A small temperature probe was integrated into the chip to measure the actual temperature sensed by the cells. (B) Temperature calibration curves. The stage and objective temperatures follow the set temperature. The sample temperature was determined to be 0.5°C below the set temperature over the range 30°C to 45°C. This difference was independent of media flow through the device. (C) Kinetics of temperature change during TS from 30°C to 38°C. Line colors are as indicated for (B) except the orange curve displays the drift in sample z-position following the change in temperature. Curves represent the means of 5 independent experiments. (D) Comparison of different heating methods to achieve a TS from 30°C to 38°C. Both stage and objective heating is necessary to ensure a reliable sample temperature.

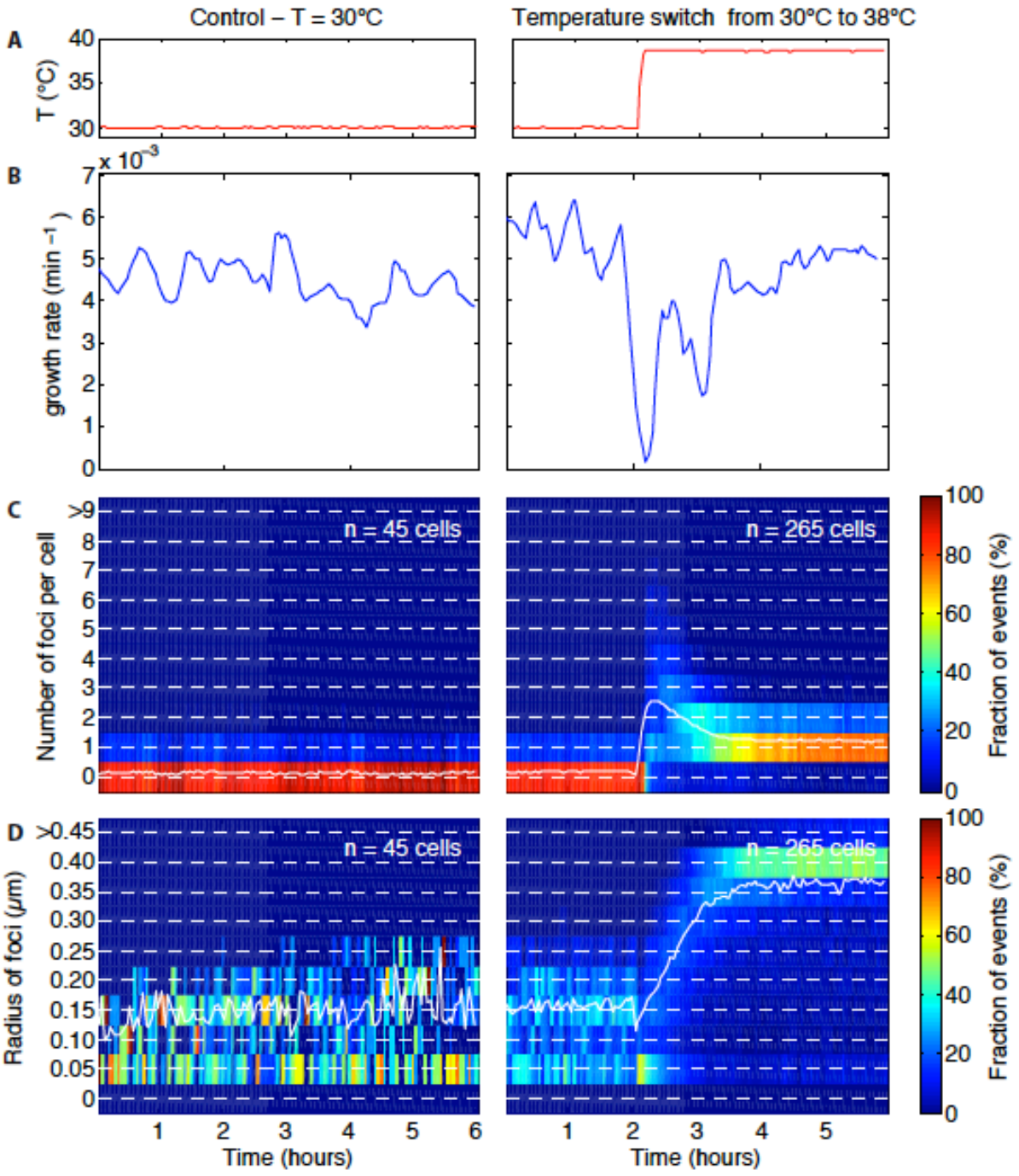

Figure S2. Comparison of foci induction and growth at 30°C and 38°C

(A) Recorded temperature of the stage. (B) Growth rate of the cell cluster. Growth rate is constant at 30°C (left) but decreases immediately after the TS to 38°C before recovering ~2 h later (right). (C) 2D histogram of the evolution of foci number per cell with time. The white line represents the mean value for the indicated number of cells. At 30°C, cells contain very few foci; mean = 0.2 foci/cell (left). This confirms that the illumination conditions do not artificially induce foci formation. (D) 2D histogram of the evolution of foci radius with time. The white line represents the mean value for the indicated number of cells. Foci do not grow over the course of the experiment at 30°C (left), whereas the foci size increases rapidly after the TS (right).

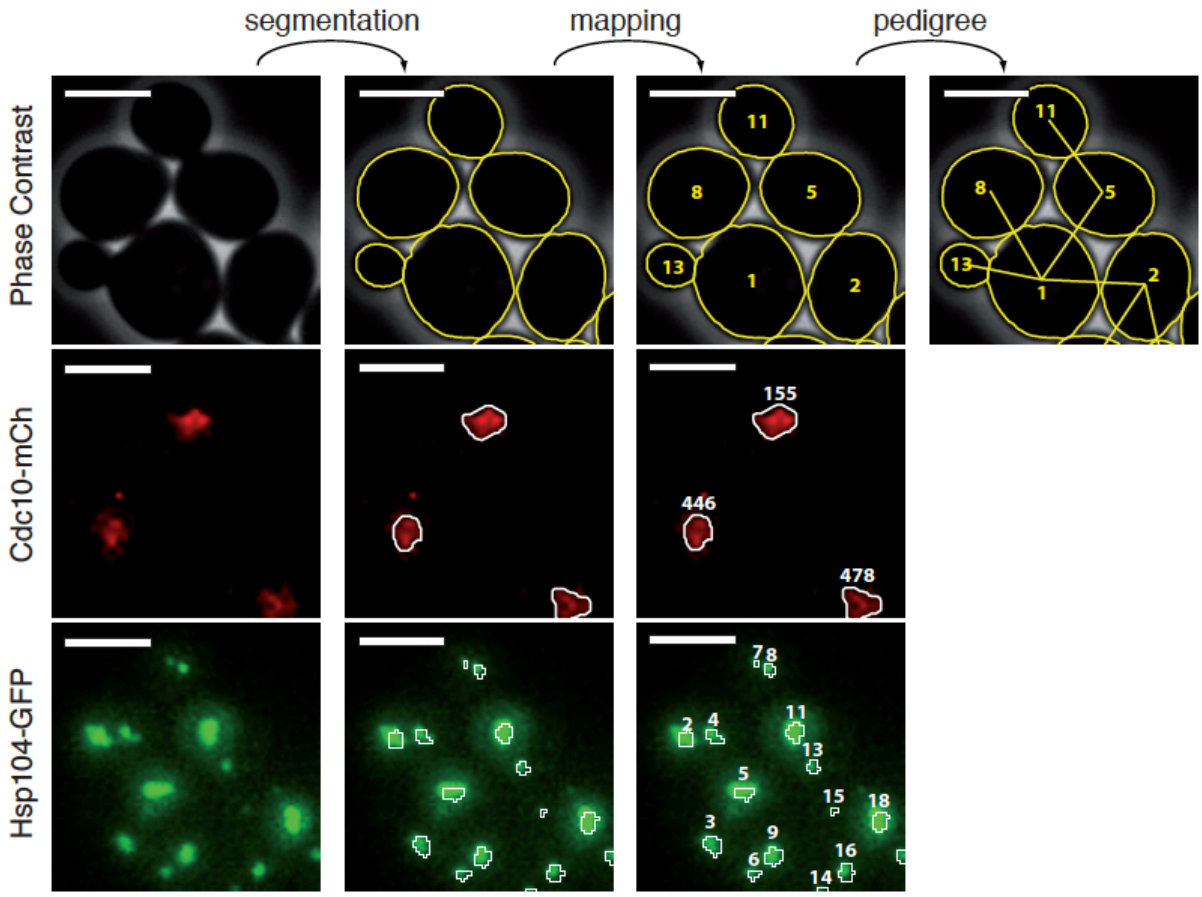

Figure S3. Image analysis pipeline

Cells (phase contrast channel), bud neck (mCherry channel), and foci (GFP channel) were automatically segmented and mapped over time by a custom-made routine. This allowed us to quantify foci features (size, number, fluorescence level), document division, follow individual cells temporally and perform pedigree analysis. The scale bar represents 4 microns.

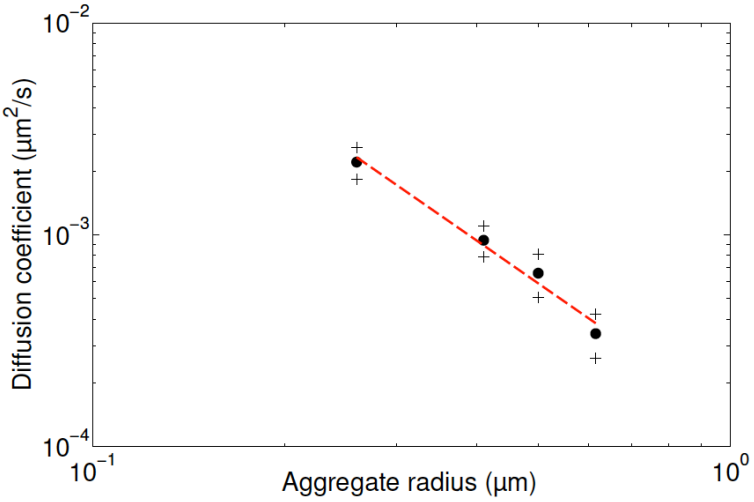

Figure S4. Aggregate diffusion coefficient as a function of size

The coefficient of diffusion of protein aggregates (PAs) was measured using standard mean square displacement analysis of PAs induced by TS. Images were acquired every 30 s using a confocal microscope to obtain a reliable estimate. The log-log plot displays a slope of -2.1, which differs from the classical Stokes-Einstein equation (Text S1).

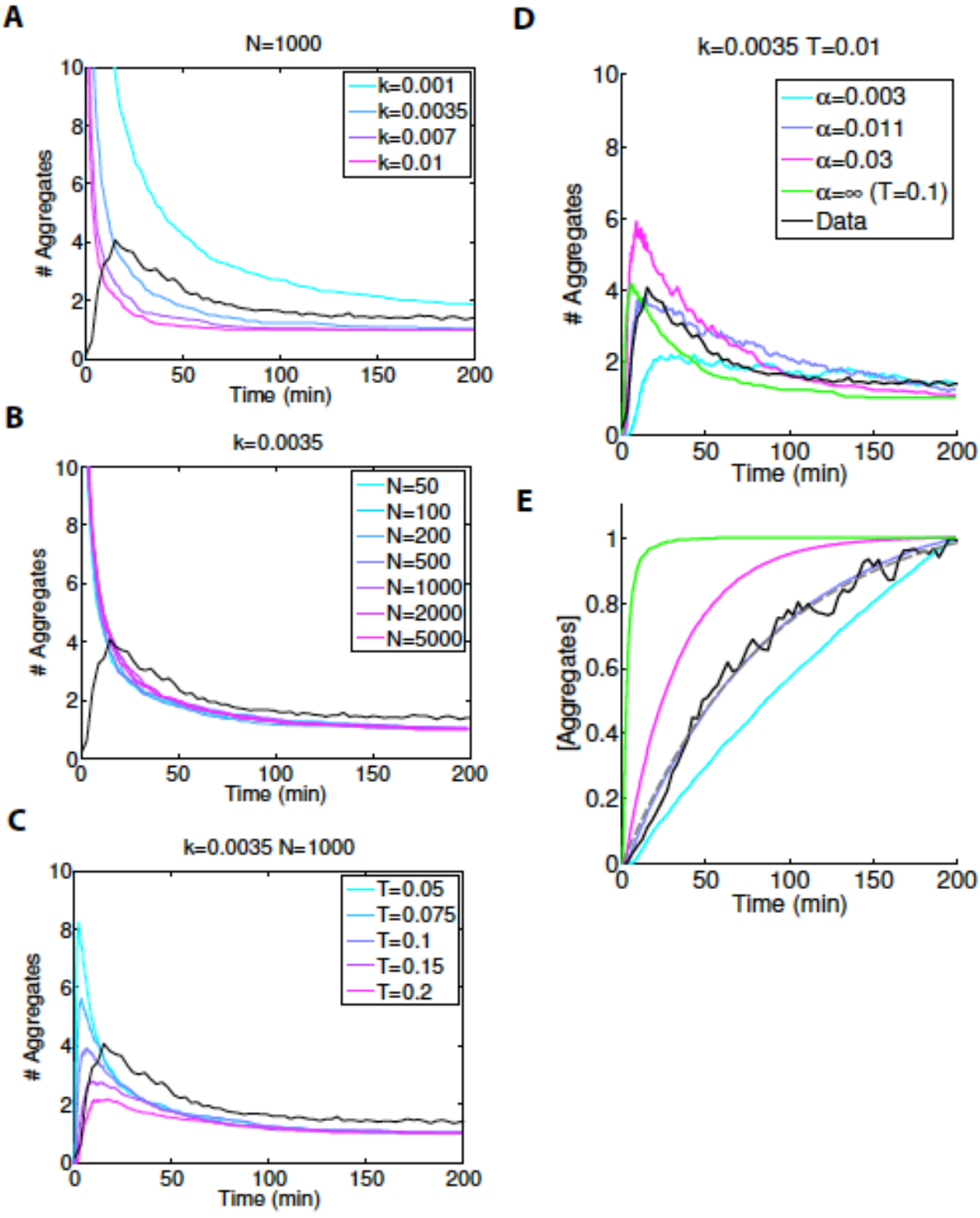

Figure S5. Effect of parameter values on the kinetics of aggregation

(A) Number of aggregates as a function of time according to the simulation described in Text S1. Each colored line corresponds to the number of PAs at the indicated value of the aggregation rate k (min^{-1}) obtained by averaging 50 runs to filter out statistical fluctuations. N is the number of initial unfolded proteins used in the simulation. The black line indicates the experimental data for the mean ± SEM number of PAs versus time observed for large mother cells (refers to Fig. 2L in the main text). (B)

Same simulation as in (A), but varying the number of initial unfolded proteins N between 50 and 5000 with a fixed value of k = 0.0035 min^{-1}. (C) Same simulation as in (A), but following the introduction of a visibility threshold T. (D, E) Same simulation as in (C), but assuming that formation of unfolded proteins follows zeroth-order kinetics with an exponential decay rate α. The number of PAs is shown in (D) and the normalized PA concentration is shown in (E). The dashed line in (E) represents an exponential fit to the experimental data (solid black line), which was used to extract the value of α.

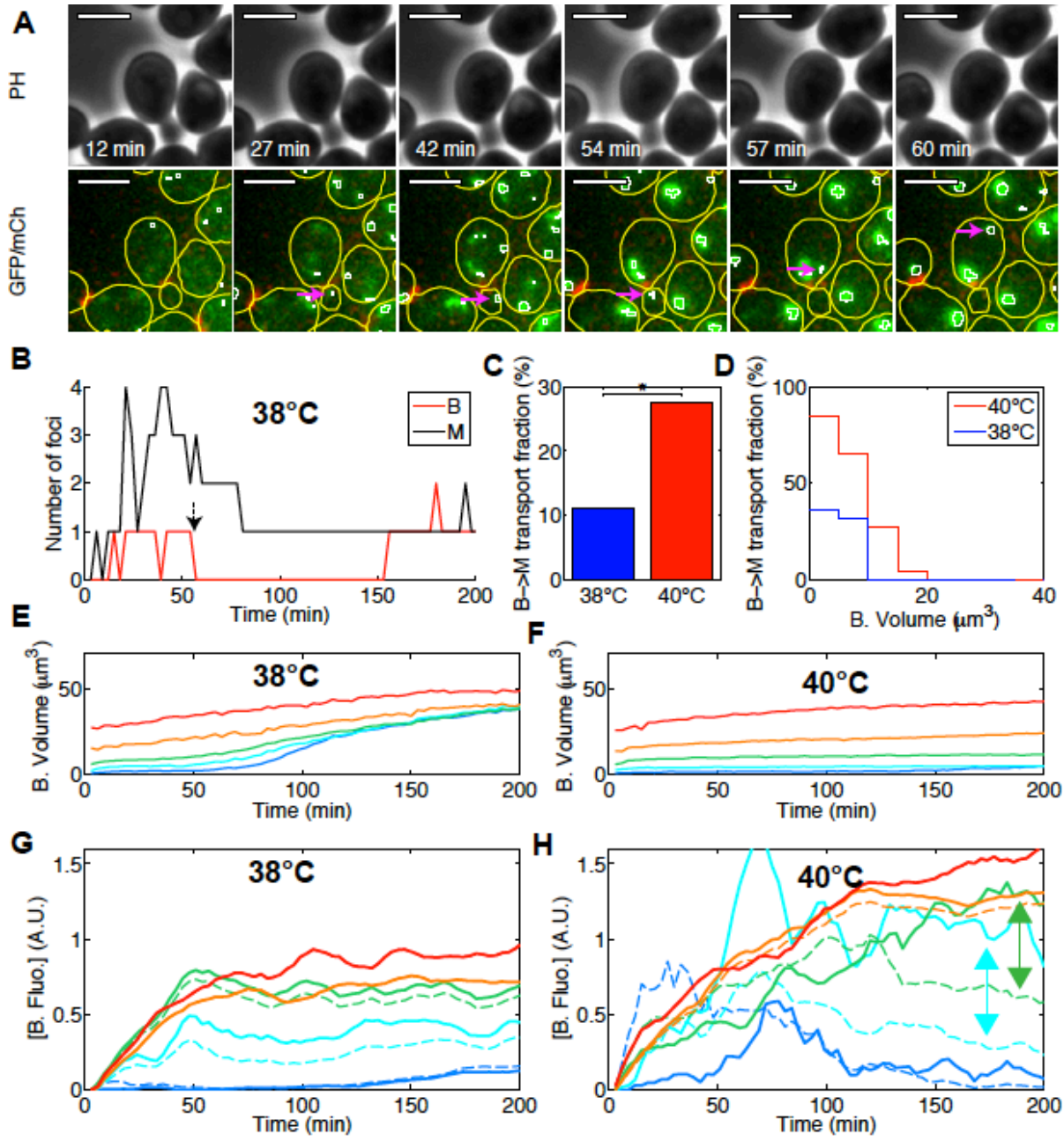

Figure S6. Bud to mother transport of aggregates

(A) Image sequence (phase contrast, overlaid Hsp104-GFP and Cdc10-mCherry fluorescence) acquired at the indicated time-points. Yellow and white lines indicate contours of the cells and Hsp104-GFP foci, respectively. Scale bar: 4 µm. Pink arrows indicate the transport of a PA from a bud

to its mother. (B) Quantification of the number of foci as a function of time for the mother (M) /bud (B) pair displayed in (A). The dashed arrow indicate the time at which a transport event occurs. (C) Fraction of cells in which a transport from bud to mother (B→M) occurs during the course of the experiment at different temperature. (D) Fraction of cells with B→M transport as a function of initial bud volume. (E, F) Evolution with time of bud volume at indicated temperatures. Each colored line represents a group of individual time traces of mother-bud pairs grouped according to the initial bud volume v : v< 2 μm^3 (blue), 2 <v< 5 μm^3 (cyan), 5 <v< 10 μm^3 (green), 10 <v< 20 μm^3 (orange), v> 20 μm^3 (red). (G,H) Evolution of PA concentration in the buds with time. Color coding is as in (E,F). Solid (resp. dashed) lines correspond to groups of cells after (resp. without) removing cells in which a B→M event occurred.

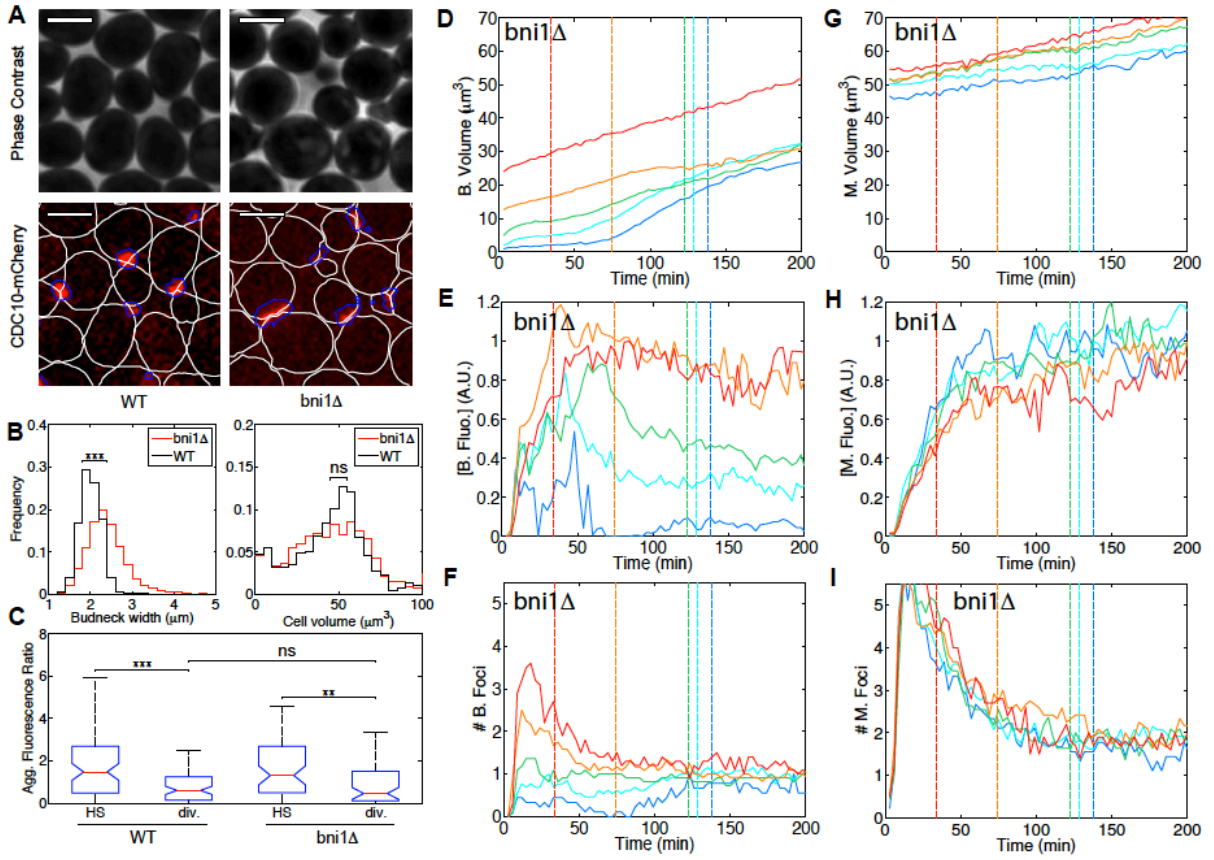

Figure S7. Asymmetric partitioning of PAs in *bni1* mutants

(A) Representative images (phase contrast and CDC10-mCherry fluorescence) of wildtype (WT, left) and *bni1*Δ (right) cells. Scale bar: 4 µm. The white lines indicate cell contours and the blue lines represent the result of bud neck segmentation (B) Left: quantification of the bud neck width following bud neck segmentation with the CDC10-mCherry marker. *Bni1*Δ mutants (red line, n = 3241 cells) display a 20% larger median bud neck width compared with WT cells (black line, n = 1080) ($p < 10^{-5}$). Right: quantification of cell size in *bni1*Δ (red line) and WT (black line) cells, indicating an insignificant difference in cell size (p = 0.89). (C) Comparison of the ratio of PA fluorescence in WT and *bni1*Δ mutants 12 minutes after TS and at division (div). There is no significant difference between fluorescence ratio in the mutant and WT at division. Both strains display a significant enrichment in

buds between TS and division. (D-I) Evolution with time of: cell size (D, G), fluorescence concentration (E, H), and number of aggregates (foci) per cell (F, I) for the bud (left column) and the corresponding mother (right column). Each colored line represents a group of individual time traces of mother-bud pairs grouped according to the initial bud volume v : v< 2 μm^3 (blue), 2 <v< 5 μm^3 (cyan), 5 <v< 10 μm^3 (green), 10 <v< 20 μm^3 (orange), v> 20 μm^3 (red). Total number of cells analyzed = 65.

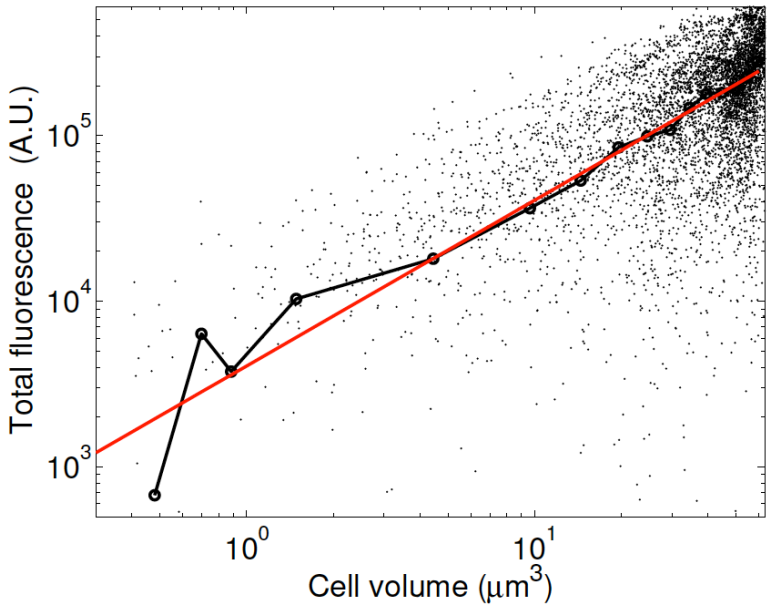

Figure S8. Scaling of fluorescence with cellular volume

Total cytoplasmic Hsp104-GFP fluorescence (sum of pixel intensities after background subtraction) within cellular compartments (including small buds) at 30°C (i.e., in the absence of foci) as a function of the volume of the compartment was calculated using the formula described in material and methods. Each point corresponds to a single cell. The solid black line represents the same data after size binning over 10 cells. The red line is a fit to the data using a powerlaw : $y=k\ x^p$ with p=1.01, indicating that normalization by cell volume is appropriate to provide a reliable estimate of concentration in cell compartments the volume of which spans several order of magnitude.

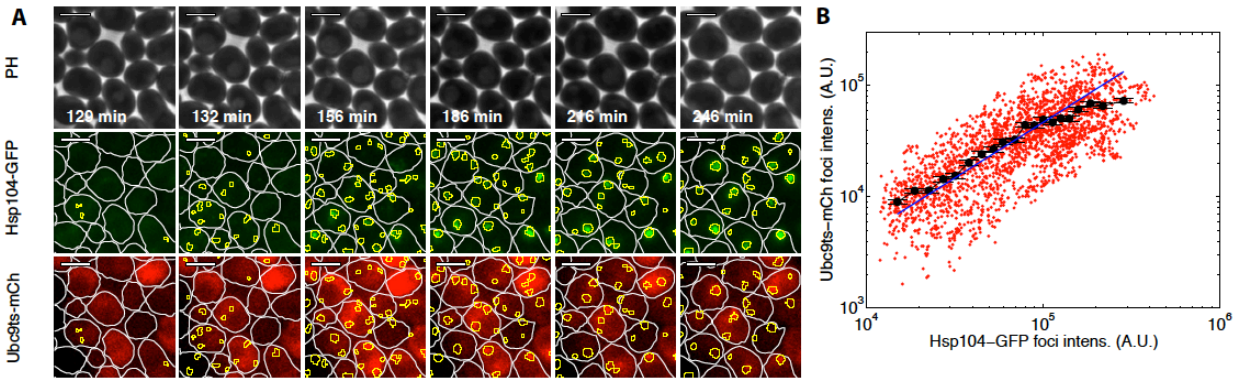

Figure S9. Scaling of Hsp104-GFP fluorescence with aggregate size

(A) Sequence of time lapse images showing the formation Hsp104-GFP and $Ubc9^{ts}$-mCherry foci following a temperature shift to 38°C (at t=120min). See material and methods for detailed

experimental procedures. The white lines indicate cell contours. The yellow contours correspond to Hsp104-GFP foci segmentation and allow one to qualitatively assess the colocalization of Hsp104-GFP with Ubc9^{ts}-mCherry. The scale bar represents 4 microns. (B) Quantification of the linearity between protein aggregation (monitored using the Ubc9^{ts}-mCherry marker) and Hsp104-GFP level. Each red dot represents the total intensity of a single focus (n >1000 foci quantified) in GFP and mCherry channels. The black dots represent binned data (over 50 points) and error bars indicate standard error on mean. The blue line represents a linear fit to the data (y = K x).

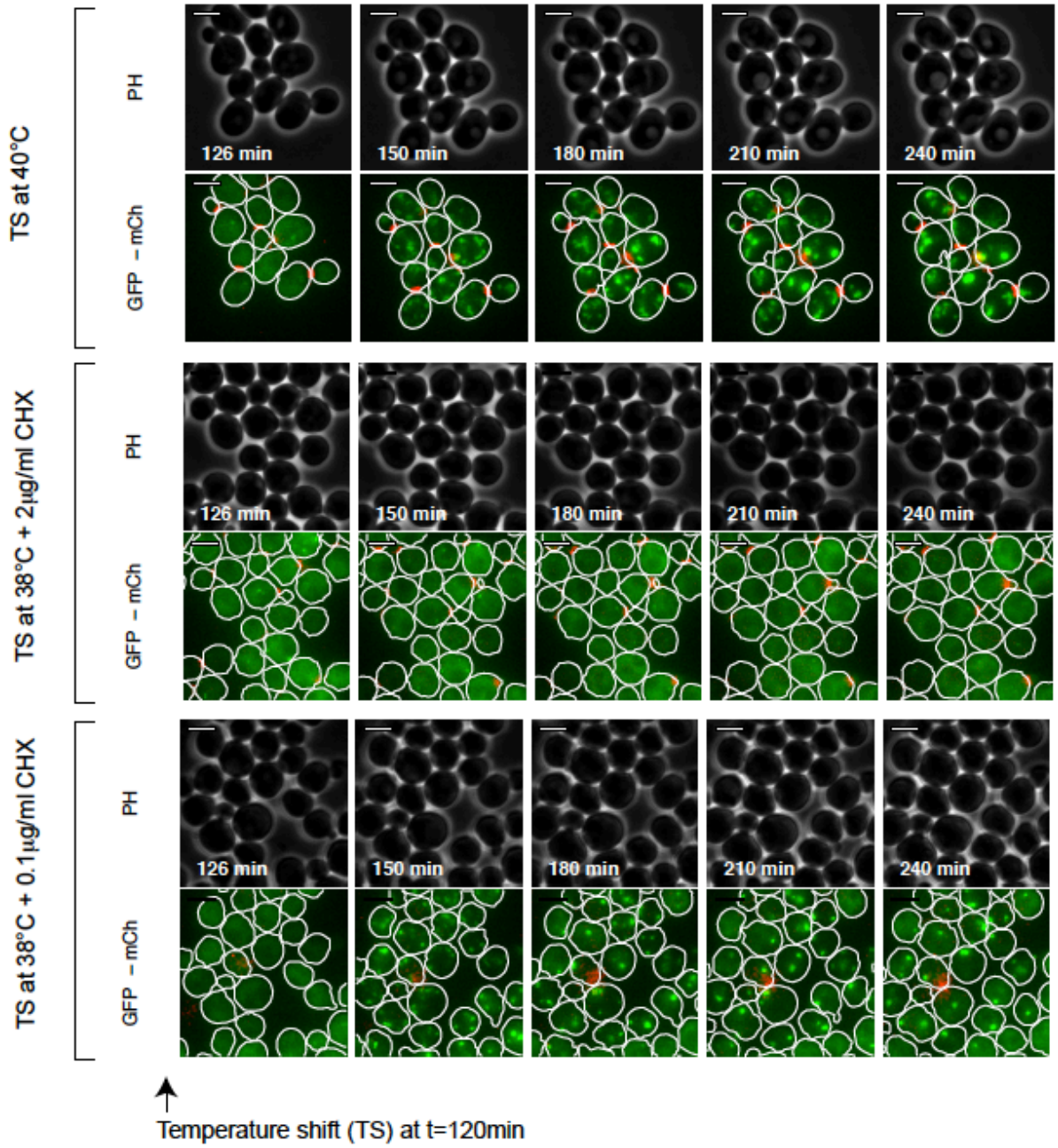

Figure S10. Perturbation of bud growth and kinetics of formation of PA

Sequence of phase contrast (PH), Hsp104-GFP and Cdc10-mCherry fluorescent images of cells following a temperature shift in the indicated conditions. The temperature shift was achieved 120 min after loading cells in the chip. White lines represent cell contours. Scale bar: 4 µm.